# BOREHOLE RADAR ATTENUATION-DIFFERENCE TOMOGRAPHY DURING THE TRACER/TIME-LAPSE TEST AT THE BOISE HYDROGEOPHYSICAL RESEARCH SITE

*Sarah E. Goldstein, Boise State University, Boise, ID*
*Tim C. Johnson, Boise State University, Boise, ID*
*Michael D. Knoll, Boise State University, Boise, ID*
*Warren Barrash, Boise State University, Boise, ID*
*William P. Clement, Boise State University, Boise, ID*

## Abstract

A tracer test and time-lapse radar imaging experiment was conducted at the Boise Hydrogeophysical Research Site to investigate the utility of crosswell radar in imaging an electrically conductive tracer plume. A multilevel water sampling system down gradient from the tracer injection well and in the radar imaging plane was used to collect detailed, 1-dimensional, fluid electrical conductivity data during the tracer test. We compare the spatial and temporal position and concentration variations of the plume as indicated by the fluid conductivity data to those suggested by radar level run attenuation differences, shot-receiver attenuation difference crossplots, and an attenuation-difference tomogram. We find that attenuation differences generally correlate well with changes in fluid conductivity. Where correlations are not so strong, the discrepancies can be explained by the difference in support volumes for the radar and chemistry measurements, and also by regularization of the radar tomogram. Our results indicate that crosswell radar imaging coupled with hydrologic tracer testing can provide useful information about subsurface fluid flow and mass transport in complex fluvial aquifers.

## Introduction

To effectively mitigate subsurface contamination problems, one needs a good understanding of the factors controlling subsurface flow and transport. Traditional subsurface characterization and monitoring methods such as core analysis, hydraulic well testing and water sampling, provide valuable information at some locations and scales, but these methods generally do not provide sufficient information to reliably and accurately predict flow and transport behavior at sites with complex hydrogeology. Geophysical methods can provide dense, high-resolution information about subsurface structures and material properties between and away from boreholes. However, the reliability and accuracy of geophysical images, and maps of hydrogeologic properties derived from these images, can be difficult to assess and quantify due to the non-uniqueness of geophysical inverse problems and the complexities of petrophysical relationships between geophysical and hydrogeologic parameters. For this reason, geophysical data are generally treated as "soft" data, with varying degrees of uncertainty, for conditioning flow and transport models (Poeter and McKenna, 1995).

There is growing awareness that many of the challenges associated with characterizing and monitoring subsurface flow and transport processes can be overcome by time-lapse geophysical imaging (e.g., Brewster and Annan, 1994; Ramirez et al., 1996; Hubbard et al., 1997; Lane et al., 1998; Slater and Sandberg, 2000; Versteeg et al., 2000; Day-Lewis et al., 2002). Differences in geophysical data or images acquired at different times may be due to experimental error, differences in the ambient noise

fields at the different times, or differences in the signals received from subsurface targets of interest, such as zones with moving or degrading contaminant plumes. If signal differences are greater than experimental error and noise differences, then time-lapse imaging has the potential to directly detect and map changes in subsurface fluid properties and distributions.

In this paper, we test the idea that time-lapse crosswell radar methods can be used to detect and image the movement of conductive fluids in fresh-water saturated, coarse, fluvial sediments. In 2001, we conducted a saline tracer test in the saturated zone at a well-characterized site, the Boise Hydrogeophysical Research Site (BHRS), where much is known about subsurface hydraulic property distributions. At the same time, we acquired time-lapse crosswell radar data across several monitoring planes that cut across the expected path of the tracer, including two planes that intersect a multilevel sampling well. We show that changes in radar amplitude values are well correlated in both time and space with changes in fluid conductivity observed at the sampling well. This suggests that time-lapse crosswell radar methods can indeed be used to detect and image the movement of saline fluids in such coarse, fluvial aquifers.

In the next section, we present some background information about the BHRS and the 2001 tracer test. Then we describe the crosswell radar imaging methods, which included both level run surveys and crosswell tomography surveys. Finally, we present results of the time-lapse imaging experiment, and compare these results to the fluid conductivity data collected at the multilevel sampling well in the middle of the radar imaging plane.

## Background

### *Site Overview*

The Boise Hydrogeophysical Research Site (BHRS) is a research wellfield located on a gravel bar adjacent to the Boise River, about 15 km from downtown Boise, Idaho (Barrash and Knoll, 1998). The wellfield consists of 18 wells: 13 wells in a central area about 20 m in diameter, and another five wells located 10-35 m from this central area. A map of the tracer test area near the center of the wellfield is shown in Figure 1. All the wells at the site fully penetrate a shallow, unconfined, fluvial aquifer that is about 20 m thick and is underlain by a tight red clay unit. The water table in the central area is typically about 2-3 m below ground surface, depending upon river levels which are controlled by a nearby dam. The wells are constructed with 4-inch ID PVC and are screened over the full saturated thickness (17-18 m) of the aquifer.

Continuous core samples collected at the site show that the aquifer is comprised of late Quaternary, coarse, fluvial deposits, dominantly mixtures of cobble, gravel and sand (Reboulet and Barrash, 1999). A variety of different hydrologic and geophysical methods have been used to investigate the hydrostratigraphy of the aquifer, including hydraulic well tests, well logging, vertical seismic and radar profiling, surface radar reflection imaging, and crosshole radar and seismic tomography (e.g., Clement et al., 1999). Based on the neutron-porosity logs, and corroborated by vertical seismic profiling and 3-D radar reflection imaging (Peretti et. al., 1999), Barrash and Clemo (2002) proposed a hierarchical model for the hydrostratigraphy of the BHRS. The model consists of five sub-horizontal units that exhibit different porosity statistics and can be traced throughout much of the central area of the wellfield, and several smaller-scale units that also appear to be distinct sediment bodies. We used this knowledge of the hydrostratigraphy at the site to design the tracer test and time-lapse radar imaging experiment.

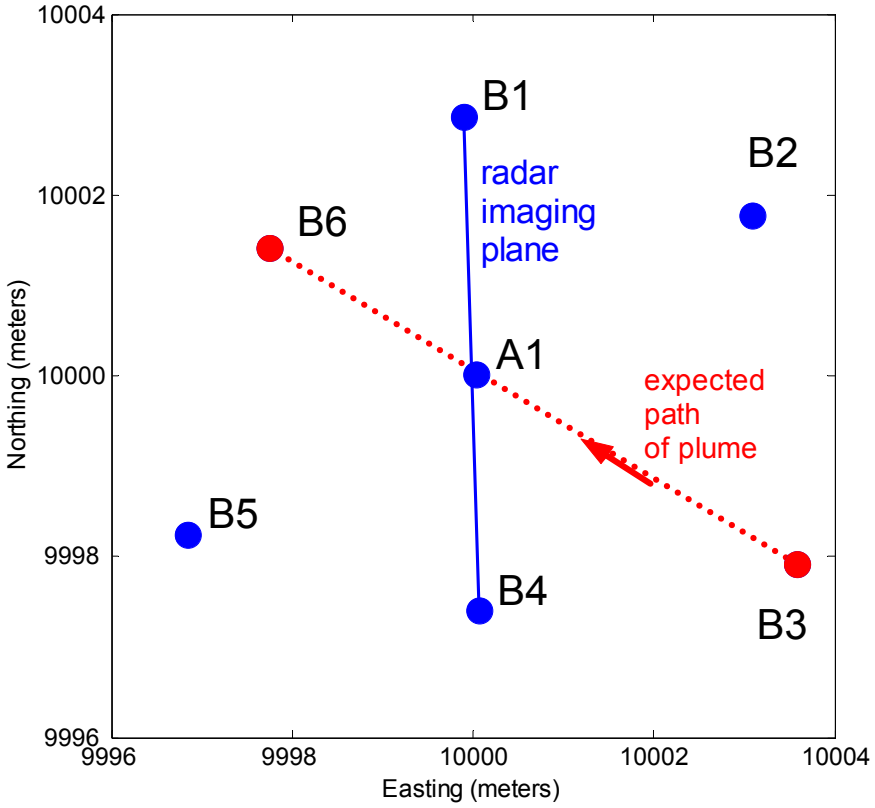


**Figure 1.** Map of the central portion of the BHRS showing the injection well (B3), the withdrawal well (B6), the twenty-zone multilevel sampling well (A1), and the surrounding monitoring wells (B1, B2, B4, B5, and B6) with log-through capability. The distance between wells B1 and B4 is 5.57 m; the distance between wells B3 and B6 is 6.90 m.

***Tracer Test Overview***

The tracer test was designed to investigate flow and transport through two units with different hydraulic properties. Our hypothesis was that the saline tracer would move at different velocities in the two units, and hence it would be a temporally and spatially varying target for time-lapse radar imaging. Following is a brief description of the tracer test; for a more detailed description see Barrash et al. (2002; 2003).

Figure 1 shows the general layout of the tracer test and time-lapse radar imaging experiment. The basic idea was to inject saline tracer into a 4-m zone of the aquifer at well B3, pump gently in a down-gradient well (B6), and monitor fluid conductivity in a short-spaced multilevel sampling well (A1) located between the injection well and the withdrawal well, as well as in some surrounding wells (B1, B2, B4, B5, B6, and C-ring wells). At the same time, we sought to monitor the tracer injection and migration processes using time-lapse crosswell radar imaging methods. To make this possible, we installed log-through packers (Barrash et al., 2002; Shapiro et al., 1999) in all the B-ring wells except the injection well (B3). Each of these packers had six, 1-m long, sampling intervals that extended across the injection interval. Well A1 was also instrumented with a multilevel packer assembly, but this assembly did not have log-through capability. Instead, this assembly isolated 20 zones, spaced 0.25 m apart across the injection interval, for chemical sampling and hydraulic head measurements.

The injection took place on August 1, 2001, and lasted about 33 minutes. Approximately 3700 liters of 7800 parts per million potassium bromide (KBr) solution were injected into well B3 between 841 and 837 m elevation (9.21 – 13.21 m below measurement point, BMP, in well B3). This 4 m interval straddles the contact between a higher porosity, higher permeability unit (Unit 2, ~11.6-15.6 m BMP) and an overlying lower porosity, lower permeability unit (Unit 3, ~8.7-11.6 m BMP). In order to ensure that the plume passed through well A1 in a reasonable time (within two weeks), we pumped well B6 at ~20 liters/minute over the course of the test.

Every four hours or so after the injection, for the next 17 days, the tracer test team collected and analyzed water samples from all the sampling intervals in well A1 and the surrounding B-ring wells. Fluid conductivity measurements were made for each water sample and plotted as a function of location and time (Hausrath et al., 2002). In this way, we sampled the movement of the bromide plume and obtained a form of ground truth for the crosswell radar imaging experiment.

We also monitored the injection and migration processes using time-lapse crosswell radar methods. During the injection, we used two different borehole radar systems (Mala; Sensors and Software) to acquire time-lapse level runs (zero-offset gathers) and select multi-offset gathers for two imaging planes (C3-B2 and B4-C2) that intersect the injection well. Immediately following the injection, we conducted dense tomography surveys for these planes in an effort to characterize the shape and dimensions of the early-time plume. We then shifted our focus to the down-gradient area and conducted time-lapse level run and tomography surveys on a daily basis across the B4-B2 and B4-B1 planes, using Mala 250 MHz and 100 MHz antennas respectively, and several level run and tomography surveys later in the test across the B3-B6 plane, using Sensors and Software 100 MHz antennas. In this paper, we focus on the temporal and spatial changes observed in the Mala 100 MHz crosswell radar data collected for the B4-B1 plane. Additional details about the radar sampling protocol and the tomographic imaging method are included in the next section.

## Methods

### *Fluid Conductivity*

Fluid conductivity data were collected during the tracer test for all the wells shown in Figure 1. In this paper, we focus on the fluid conductivity data for well A1. Fluid conductivity was measured in the field with an Accumet AR50 conductivity meter and probe (range 10-2000 μS/cm). Temperature was measured with a Traceable thermometer. Since fluid conductivity is a function of temperature, we corrected all conductivity measurements to a common temperature (25 degrees C) for comparison purposes. Additional details about the sampling protocol, the conductivity measurement method, and the temperature compensation procedure may be found in Hausrath et al. (2002).

### *Crosswell Radar*

We used a Mala Geosciences RAMAC borehole radar system with 100 and 250 MHz antennas to image the B4-B1 plane before, during, and after the tracer test; in this paper we focus on the 100 MHz time-lapse data. We conducted level run and tomographic radar surveys of the B4-B1 plane. The level run surveys sampled the subsurface every 0.1 m in depth. We collected the tomographic data with the receiver (fixed antenna) in well B1 and the transmitter (slowly moving antenna) in well B4. The receiver spacing was 0.2 m and the transmitter spacing was 0.05 m; we used the moving transmitter and an encoder wheel to trigger the radar system. Each trace consisted of 480 samples collected over 225.5

ns and stacked 64 times. We collected airwave records and surface walkaways before and after each tomographic survey to check the stability of the timebase and to calibrate time zero.

The radar data required some pre-processing before attenuation analysis. First, we had to de-clip approximately 20% of the traces (mostly near-level rays above 10 m depth) to recover lost amplitude information. The de-clipping algorithm uses spline interpolation to estimate clipped amplitude values. Testing of this algorithm on artificially clipped traces showed that, in most cases, the reconstructed amplitude was within 5% of the true amplitude. We then removed the zero-frequency amplitude bias of the data by calculating the mean amplitude of the samples before the direct arrival and subtracting this value from each data point. Examining the result for samples before the first arrivals, we determined that the noise level of the data is approximately ±50 amplitude units (au). To avoid having to manually pick amplitude values for the direct arrivals of many thousands of traces, and to reduce sensitivity to noise, we decided to work with trace energy as our tomography data parameter. To compute trace energy, we summed the squared amplitudes of all samples with a magnitude greater than the noise level. The data with source-receiver separations greater than 9 m had relatively low signal-to-noise ratios, so we only used data with separations less than this (ray coverage less than 54 degrees) in the tomographic inversions.

### *Tomographic Inversion*

Attenuation tomography involves measuring amplitude values for waves that propagate along many different raypaths through a medium, and then inverting these data for the attenuation structure of the medium. There are several decisions that one must make to implement attenuation tomography. First, one must decide on the form of the data. One can use the amplitude of first arrivals (e.g., amplitude of first peak or trough, or their difference) (Zhou and Fullagar, 2001; Holliger et al., 2001), energy computed over some time interval (e.g., sum of squared amplitudes over the wavelet period or the entire trace) (Lane et al., 2000), or some measure of pulse broadening such as the centroid frequency of the amplitude spectra (Quan and Harris, 1997; Liu et al., 1998). Second, if time-lapse data are available, one must decide between attenuation tomography, which involves inverting each dataset separately and then differencing the models (Zhou et al., 2001; Liu et al., 1998), or attenuation-difference tomography, which involves differencing the data and then inverting for the change in the model parameters (Lane et al. 2000, Day-Lewis et al., 2002). After considering the different methods and forms of data that could be used in tomographic analysis of the time-lapse radar data, we chose to use attenuation-difference tomography with trace energy as the fundamental data for this study.

From the 1-D solution to the electromagnetic wave equation, we can estimate the attenuation of a radar wave propagating through a medium. We assume straight rays, which is a reasonable assumption given the small radar velocity variations in the saturated zone at the BHRS (Clement et al., 1999). For straight rays, the amplitude of the electric field ($A$) recorded by a dipole antenna in a crosswell survey is related to the transmitted amplitude ($A_o$) by:

$$A = \frac{A_o e^{-\alpha l} \theta_T \theta_R}{l} \tag{1}$$

where $\alpha$ is the attenuation coefficient in nepers per meter (Np/m), $l$ is the length of the raypath in meters, and $\theta_T$ and $\theta_R$ are dimensionless scale factors that account for the radiation pattern and coupling effects of the transmitter and receiver antennas, respectively. We calculate the energy of a radar trace by integrating (or summing) the squared amplitude values over the recording time:

$$E = \int A^2 dt = \int \frac{A_o{}^2 e^{-2\alpha l} \theta_T{}^2 \theta_R{}^2}{l^2} dt \tag{2}$$

Equation (2) can also be written in terms of the transmitted energy ($E_o$):

$$E = \frac{E_o e^{-2\alpha l} \theta_T{}^2 \theta_R{}^2}{l^2} \tag{3}$$

If we have traces recorded at two different times for the same source and receiver locations, and if we assume that the raypaths and antenna scale factors are time invariant, then we can write:

$$\frac{E_1}{E_2} = \frac{E_{1,o} e^{-2\alpha_1 l}}{E_{2,o} e^{-2\alpha_2 l}} \tag{4}$$

where $E_1$ is the energy at recording time 1, and $E_2$ is the energy at recording time 2. If we further assume that the transmitted energy is the same at the two recording times ($E_{1,o}$=$E_{2,o}$), then equation (4) simplifies to:

$$\frac{E_1}{E_2} = e^{-2(\alpha_1 - \alpha_2) l} \tag{5}$$

We linearize equation (5) by taking the natural logarithm of each side, and then we discretize $l$ and integrate along the raypath.

$$\frac{1}{2} \ln\left(\frac{E_1}{E_2}\right) = -\int_{raypath} (\alpha_1 - \alpha_2) dl \tag{6}$$

Equation (6) relates the change in trace energy observed at two different recording times for a given transmitter-receiver pair to the changes in attenuation coefficient values along the raypath. We refer to the left-hand side of equation (6) as the attenuation difference, $d$, and calculate this parameter from the recorded radar data as follows:

$$d = \frac{1}{2} \ln\left(\frac{\sum^{nsamps} A_1{}^2}{\sum^{nsamps} A_2{}^2}\right) \tag{7}$$

where $A_1$ and $A_2$ are the amplitudes of the samples collected at recording times 1 and 2, respectively, and *nsamps* is the number of samples in each trace. The attenuation differences for each transmitter-receiver pair then become the data vector, **d**, in the tomographic inverse problem.

Equation (6) can also be discretized and written as a linear system of equations. The weighted, damped, least-squares solution of this system is given by (Menke, 1989):

$$\mathbf{m} = \langle \mathbf{m} \rangle + [\mathbf{G}^T \mathbf{W_d} \mathbf{G} + \varepsilon^2 \mathbf{W_m}]^{-1} \mathbf{G}^T \mathbf{W_d} [\mathbf{d} - \mathbf{G} \langle \mathbf{m} \rangle] \quad (8)$$

where **m** is the vector of changes in attenuation coefficients ($\Delta\alpha=\alpha_1-\alpha_2$), **<m>** is the a priori vector of model parameters, **G** is the matrix containing the lengths of each ray through each cell in the model, and **d** is the vector of attenuation differences calculated according to (7). In this equation, $\mathbf{W_m}$ is the model regularization matrix, $\mathbf{W_d}$ is the data weighting matrix, and $\varepsilon^2$ is the trade-off parameter that controls the extent to which the solution minimizes prediction error and the model norm. In the inversions shown in this paper, we weighted data equally ($\mathbf{W_d}$ equals the identity matrix), regularized using a flatness constraint (isotropic smoothing), and used $\varepsilon^2=10$ (based on trial and error) to arrive at a constrained solution with reasonably small prediction error. The grid size used for the forward modeling and inversion was 0.25 m which is slightly greater than the receiver spacing and roughly one fifth the dominant wavelength of the data.

## Results

### *Level Runs*

Figure 2 shows some processed traces from the B4-B1 level run surveys (100 MHz) conducted on August 2 and 10, 2001. The paired waveforms were recorded at four depths: 6.0, 10.0, 13.0 and 17.0 m. At depths of 6.0 and 17.0 m, there is very little difference in the waveforms recorded on the two days, but at depths of 10.0 and especially 13.0 m, there are significant differences in the amplitude values recorded on the two days between 75 and 100 ns. The noise levels for both data sets are very similar, but the signal levels and dominant frequencies are clearly different for the data recorded at intermediate depths (i.e., around the injection interval). At depths of 10.0 and 13.0 m, the peak amplitude values measured on August 10 are less than they are on August 2. This can be explained by the migration of saline fluid across the B4-B1 plane between August 2 and August 10 as discussed in the next section.

To better resolve spatial and temporal changes in radar attenuation, we plotted attenuation differences, as calculated by equation (7), for all the B4-B1 level run data. The results are shown in Figure 3, where the level run data collected on August 2 are taken as the initial conditions. The hotter colors indicate that there are large changes in attenuation between 10 and 14 m depth. The changes in attenuation begin on August 6 and continue through August 15, the last day of the level run surveys. For the period August 6 through August 8, the larger attenuation differences are located between 12 and 14 m depth. Between August 8 and 10, attenuation differences are observed in two distinct zones, one zone between 10.0-11.5 m and another zone between 12-14 m depth; between these two zones (11.5-12.0 m), there is little, if any, change in attenuation over this period. After August 10, the attenuation differences occur between 10 and 14 m depth, with peak differences centered around 11.25 and 12.5 m. Above and below the depths of these two peaks, attenuation differences generally decreased with time after August 12.

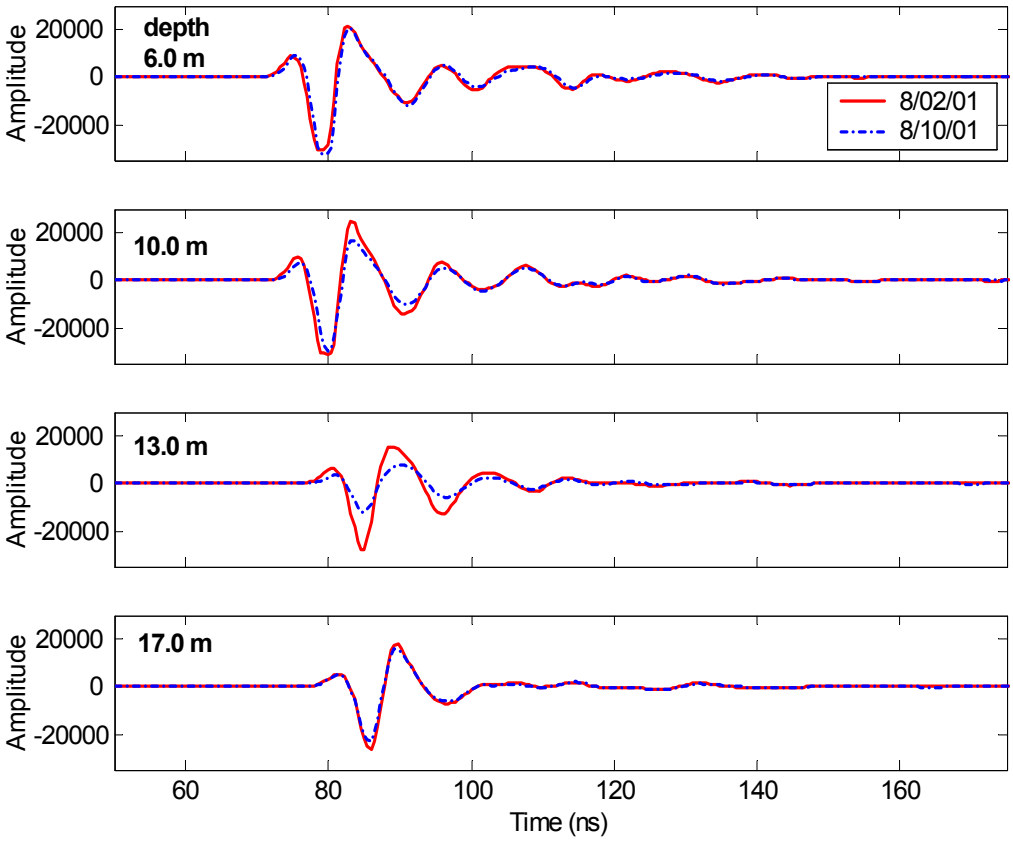


**Figure 2.** Level run traces for depths of 6.0, 10.0, 13.0 and 17.0 m recorded on August 2 and August 10, 2001.

Figure 4 shows the fluid conductivity data measured in well A1 (Hausrath et al, 2002), plotted as a function of depth and time of sampling. Note that the vertical scale, corresponding to the monitoring interval, is less than that shown in Figure 3. This plot shows breakthrough beginning at well A1 on August 7 (or August 6 if the conductivity scale is log-transformed to provide more dynamic range at the low end of the scale). Between August 7 and August 11, high fluid conductivity values are observed below 12.5 m depth. On August 11, the high conductivity zone shifts upward such that by August 12 it is located between 11.5 and 13.0 m depth. The zone between 11.5 and 13.0 m depth continues to exhibit high fluid conductivity values through August 15, at which time the conductivity quickly drop offs to levels near background (200 µS/cm).

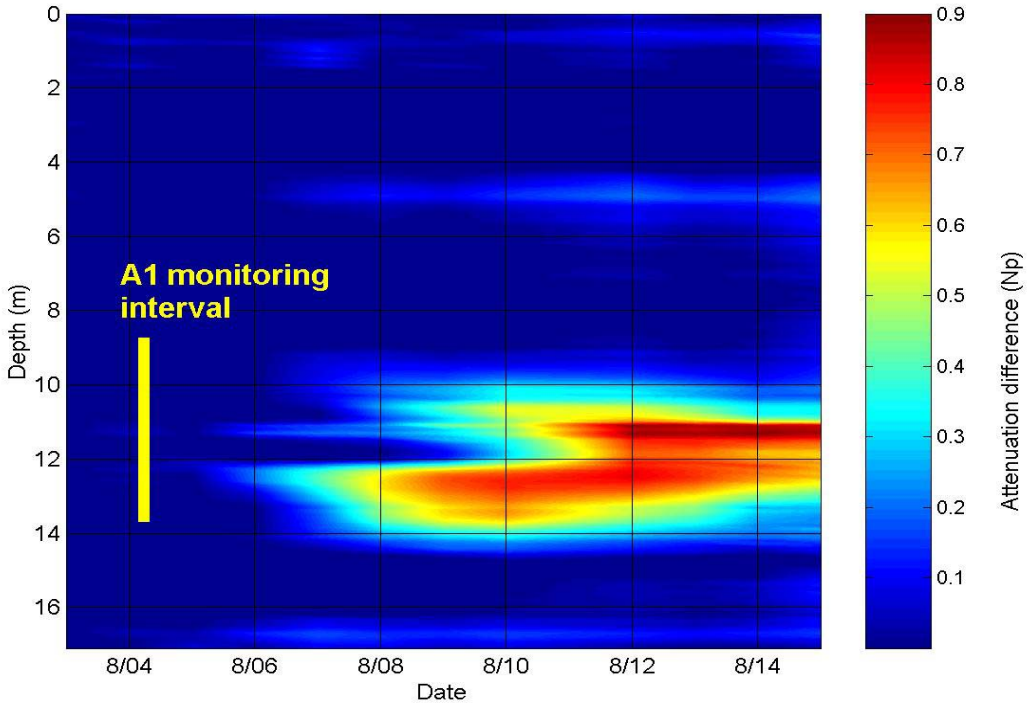


**Figure 3.** Attenuation differences for the time-lapse level run surveys (100 MHz) of the B4-B1 plane. The differences were calculated using equation (7). Data from August 2, 2001, were used as the initial conditions.

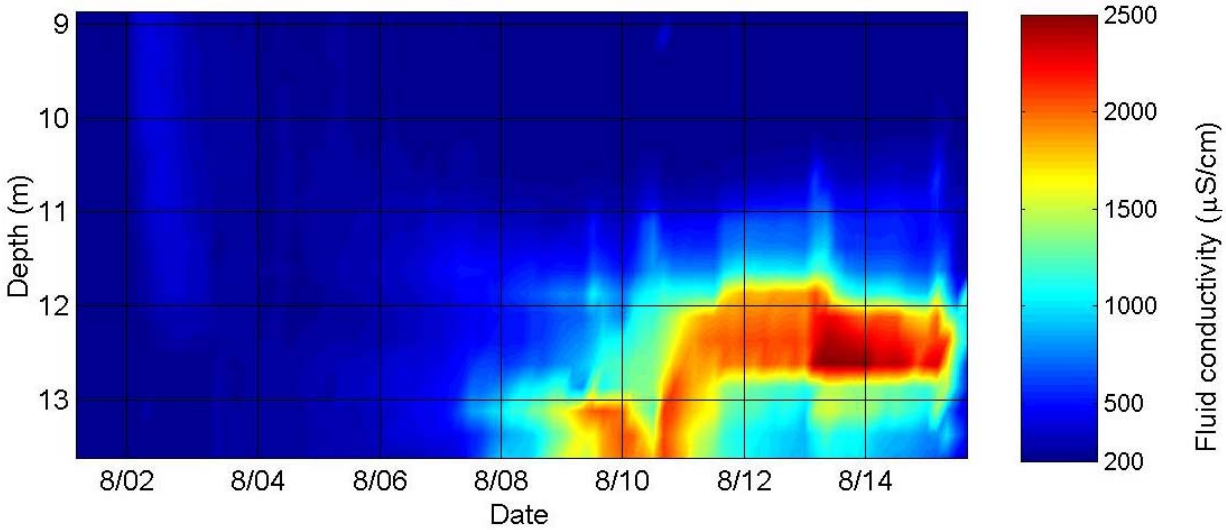


**Figure 4.** Fluid conductivity for water samples collected in well A1 (after Hausrath et al., 2002). The samples were collected from 20 zones spaced 0.25 m apart over the monitoring interval (8.75-13.75 m depth). Conductivity values have been temperature-compensated to 25 degrees C.

***Tomography***

Although the level run surveys show that attenuation varies with time and depth, these surveys provide no real lateral resolution within the imaging plane. To image the bromide plume in the B4-B1 plane, we use attenuation-difference tomography. We begin by constructing and comparing trace energy crossplots for the data we plan to difference and invert.

Figure 5 displays the trace energy crossplots for the B4-B1 100 MHz tomography data sets collected on August 2 (left plot) and August 10 (right plot). Trace energy values, computed using equation (2), are plotted as colors on the grid of source and receiver locations. These energy crossplots are useful for examining the attenuation structure of the plane. Regions in the plots displaying low energy indicate that radar waves are highly attenuated along these raypaths; conversely areas with high energy indicate that waves are not heavily attenuated along these raypaths. Overall, the trace energy values on August 2 are larger than those on August 10, indicating that the energy traveling through the B4-B1 plane on August 10 was more strongly attenuated than the energy traveling through on August 2. The two images differ significantly in the region in which both the transmitter and receiver are below 11 m depth; here we notice regions centered at approximately 11.5, 13, and 14 m depth in which the trace energies are significantly higher on August 2 than on August 10. The depths of these differences correspond to regions where the level run data also indicated attenuation changes (Figure 3).

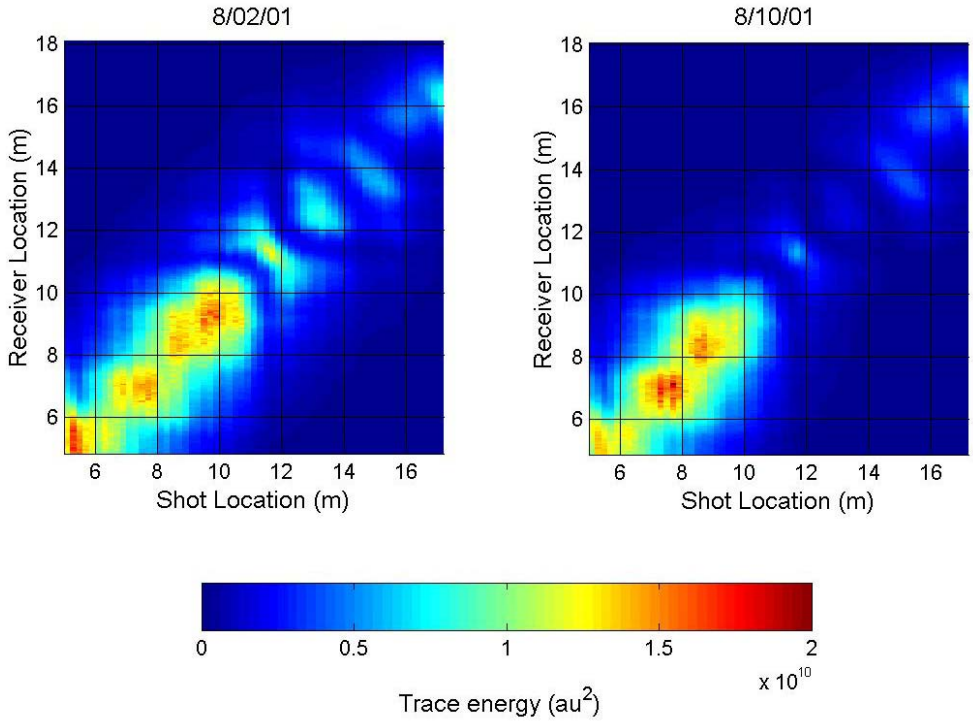


**Figure 5.** Trace energy on August 2 and August 10, 2001, plotted as a function of transmitter and receiver depths. The level run data fall along the diagonal from the lower left to the upper right. The colorbar indicates the magnitude of trace energy.

In Figure 6, we examine the attenuation differences between August 2 and August 10 for each transmitter-receiver pair. This crossplot indicates that the changes in attenuation of waves traveling only above 8 m depth and below 16 m depth are small compared to the changes in attenuation of waves traveling through the center of the plane. Additionally, we see the largest changes in attenuation occur in the higher angle rays, i.e., the upper left and lower right corners of the figure. Finally, we notice that the level and near-level rays at approximately 12 m depth show small changes in attenuation.

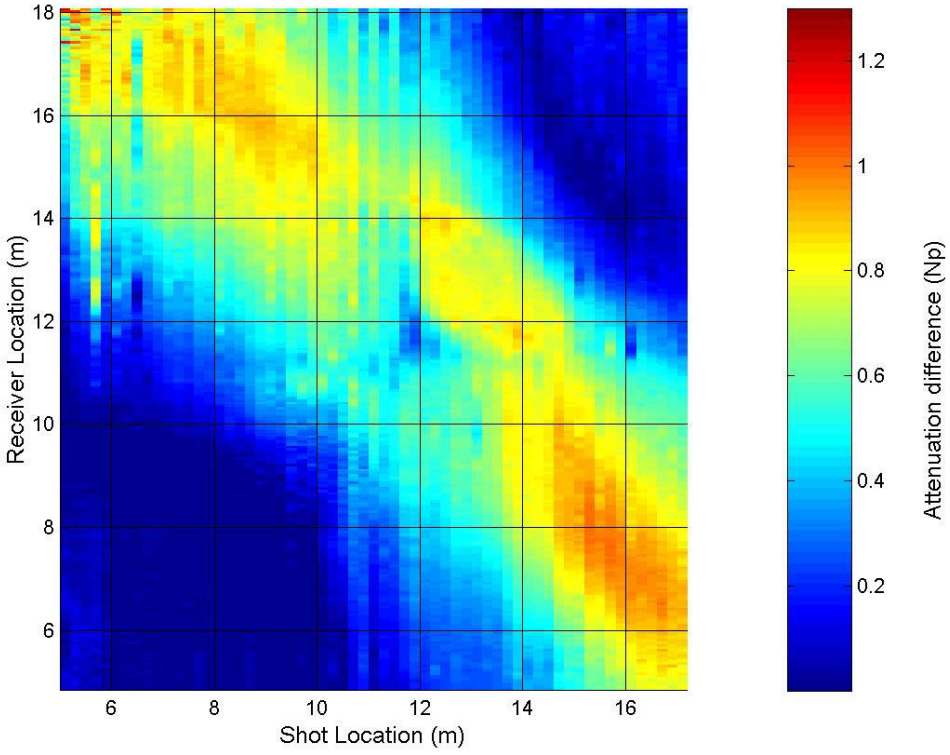


**Figure 6.** Attenuation differences between August 2 and August 10 in the B4-B1 plane plotted with respect to transmitter and receiver depths. Attenuation differences were calculated according to equation (7).

The results of tomographic inversion of the attenuation-difference data from August 2 and 10 for the B4-B1 plane are presented in Figure 7. The tomogram shows large changes in the attenuation coefficients between 10 and 14 m depth. The largest changes in the attenuation coefficients occur between 12 and 14 m depth in a zone approximately 3 m wide that is centered between wells B1 and A1 rather than at well A1 which is directly in line with the injection and withdrawal wells used in the tracer test.

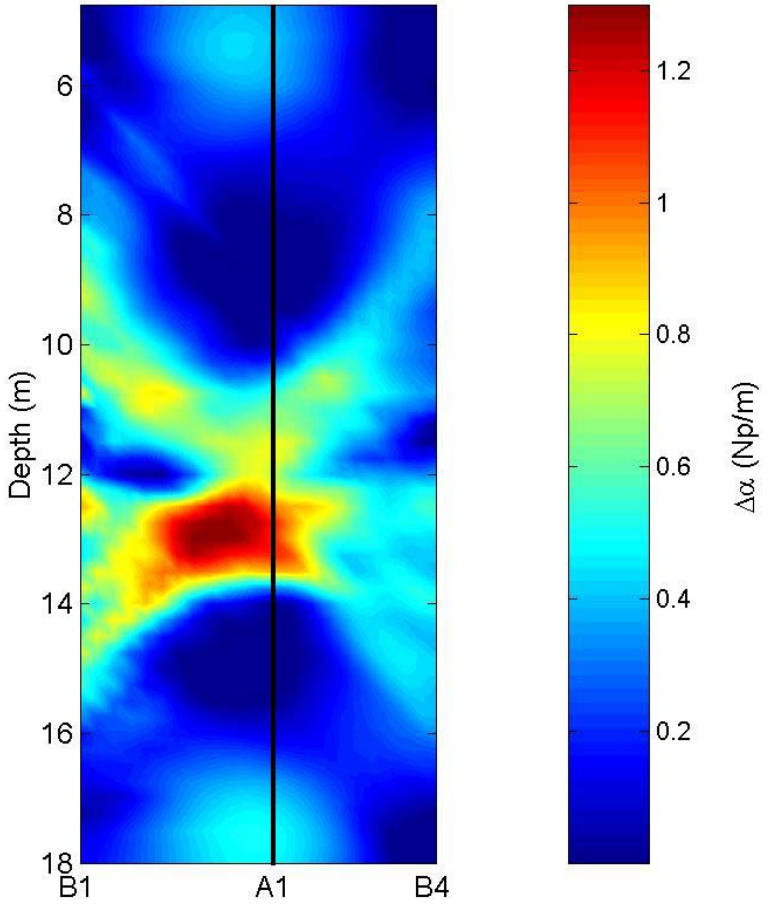


**Figure 7.** Attenuation-difference tomogram for the B4-B1 plane between August 2 and 10, 2001.

The radar image may be compared to the water chemistry data collected during the tracer test by comparing the changes in the attenuation coefficients of the column of cells that correspond to the location of well A1 with the fluid conductivity data collected there. Figure 8 displays this comparison for the changes between August 2 and August 10.

The fluid conductivity data in Figure 8 indicate the presence of the plume between 10.5 and 13 m depth in well A1 on August 10, 2001. The tomography results display large changes in the attenuation coefficients between 10 and 14 m depth in the region corresponding to well A1. The peak in fluid conductivity occurs at 12.37 m depth; the peak in the change in the attenuation coefficient occurs at 12.75 m depth. The changes in the attenuation coefficient above 8 m depth and below 15.5 m depth (Figure 8) are believed to be artifacts of the inversion (due to smearing along high angle rays and differences in ray coverage) and not true indications of changes in the attenuation coefficients in these regions.

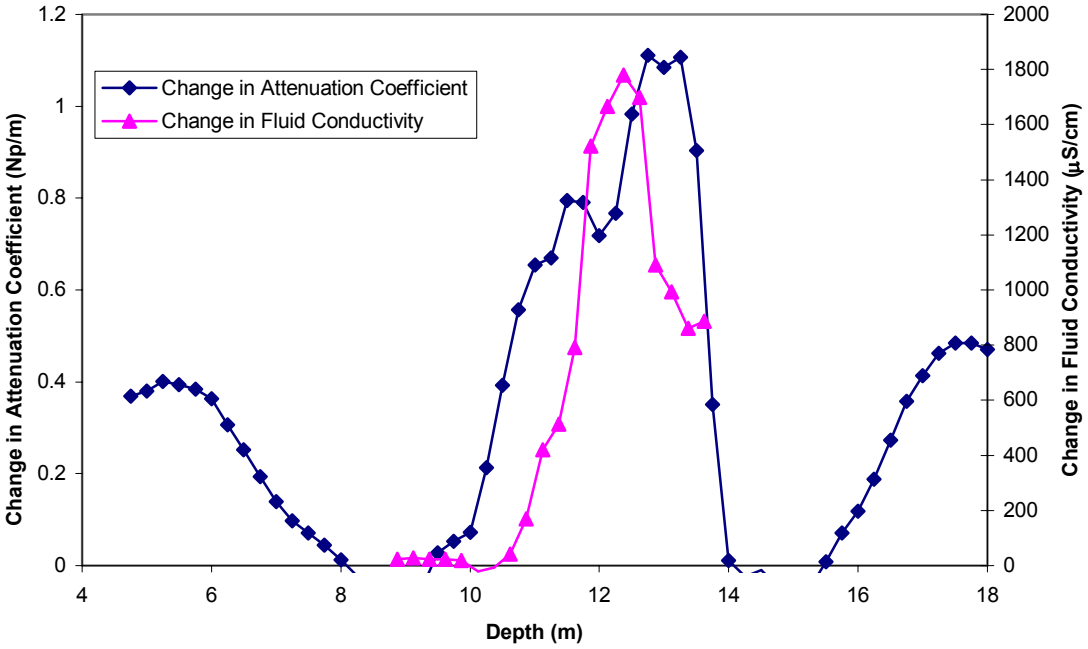


**Figure 8.** Changes in fluid conductivity and attenuation coefficient at well A1 between August 2 and August 10, 2001, plotted versus depth.

## Concluding Discussion

Results of crosswell radar imaging during the 2001 tracer test at the BHRS indicate that radar can be used to detect and image a conductive plume in the subsurface. Here, we utilize the combination of level runs, attenuation difference cross-plots, and an attenuation-difference tomogram to make an interpretation about the plume characteristics in the B4-B1 plane on August 10, 2001.

First, the plume at the B4-B1 plane appears to be traveling in two lobes on this date, with the break occurring at approximately 12 m depth. This break is most evident in the level run data and the attenuation difference cross-plot. Second, the tomogram indicates that on August 10 the lower lobe of the plume is larger and has higher conductivity than the upper lobe. The level run data also indicate the lower lobe has higher conductivity than the upper lobe.

The effects of differences in measurement scales between radar and conductivity measurements are evident in the level run analysis. The conductivity data may be considered point measurements while radar waves sample an elliptical volume over the travel path (the Fresnel volume). For instance, on all dates after breakthrough, the vertical extent of attenuation changes in the levels runs is larger than the vertical dimensions of the plume at A1 as indicated by the chemistry data collected there. Although the level run data display a 'smearing' in both time and space in comparison to the conductivity data, a good correlation exists between the temporal and spatial changes in the plume characteristics suggested by both data sets. Each data set shows breakthrough occurred in the B1-B4 plane on August 6 and also an upward shift in the depth of the conductive zone between August 10 and 12. The smearing in the level run data is likely caused by: 1) the larger sampling volume of radar wave propagation, and/or 2) the presence of the plume in the B4-B1 plane, but not in contact with well A1. Also, because radar wave

propagation samples a volume which includes material outside of the B4-B1 plane, the level run data will indicate the presence of the plume before it reaches well A1. Similarly, rays traveling above and below the plume may be attenuated due the sample volume of radar waves. Additionally, if the plume crosses the B4-B1 plane without intercepting A1, the level run data will display changes in attenuation, while chemistry data will show no conductivity changes in A1. Together, these effects may account for the discrepancies in plume characteristics as described by the level run and the conductivity data.

Attenuation difference crossplots (Figure 6) are also useful in examining the correlation between changes in radar attenuation and fluid conductivity. Figure 6 shows no significant changes in attenuation between August 2 and 10 in rays traveling only above 8 m and below 16 m depth. Careful examination of Figure 4 and Figure 6 also shows that rays displaying large changes in attenuation travel through the high conductivity zone in A1. The smearing effects of the radar sample volume described previously are also evident in Figure 6.

Tomographic inversion provides a 2-D image of changes in the attenuation structure in the B4-B1 plane between August 2 and August 10. In Figure 7, the positions of the zones with large changes in attenuation coefficients correlate well with attenuation changes displayed by the level run data. However, in Figure 8, the depth range of significant changes in attenuation coefficients at well A1 is greater than the depth range of changes in fluid conductivity in A1. Again, we attribute some portion of this smearing to the effects of volumetric radar sampling. Regularization of the inversion will also introduce some smearing of the high attenuation zone. The tomogram suggests that changes in attenuation coefficients extend to approximately 14 m depth. The chemistry data for well A1 also suggest that high fluid conductivity values may extend below 13.5 m.

## Acknowledgments

Work presented here was supported by EPA grant X-970085-01-0 and U.S. Army Research Office grants DAAH04-96-1-0318 and DAAG5-98-1-0277. Instruments and equipment acquired under grants from the U.S. Army Research Office (DAAD19-00-1-0105) and the Murdock Charitable Trust were used in support of this research. Identification of brand names for instruments is for identification purposes only and is not an endorsement for any brand by Boise State University or any of the project sponsors. Cooperative arrangements with the Idaho Transportation Department, the U.S. Bureau of Reclamation, and Ada County allow development and use of the BHRS and are gratefully acknowledged. We would also like to thank the many students and researchers who helped us in the field with the 2001 tracer test and time-lapse radar imaging experiment.

## References

1. Barrash, W., and Clemo, T., 2002, Hierarchical geostatistics and multifacies systems: Boise Hydrogeophysical Research Site, Boise, Idaho: Water Resources Research, vol. 38, no. 10, 1196, doe: 10.1029/2002WR001436, 2002.
2. Barrash, W., and Knoll, M. D., 1998, Design of a research wellfield for calibrating geophysical methods against hydrologic parameters: Proc., 1998 Conference on Hazardous Waste Research (Snowbird, UT), Great Plains/Rocky Mountain Hazardous Substance Research Center, Kansas State University, Manhattan, KS, 296-318.

3. Barrash, W., Clemo, T., Hyndman, D., Reboulet, E., and Hausrath, E., 2002, Tracer/time-lapse imaging test: Design, operation, and preliminary results. Center for Geophysical Investigation of the Shallow Subsurface Technical Report BSU CGISS 02-02, Boise State University, 120 p.
4. Barrash, W., Knoll, M. D., Hyndman, D. W., Clemo, T., Reboulet, E. C., and Hausrath, E. M., 2003 (this conference), Tracer/time-lapse radar imaging test at the Boise Hydrogeophysical Research Site: Proc., SAGEEP 2003 (San Antonio, TX), EEGS, Denver, CO.
5. Brewster, M.L., and Annan, A.P., 1994, GPR monitoring of a controlled DNAPL release: 200 MHz radar: Geophysics, vol. 59, 1211-1221.
6. Clement, W. P., Knoll, M. D., Liberty, L. M., Donaldson, P. R., Michaels, P., Barrash, W., and Pelton, J. R., 1999, Geophysical surveys across the Boise Hydrogeophysical Research Site to determine geophysical parameters of a shallow, alluvial aquifer: Proc., SAGEEP 1999 (Oakland, CA), EEGS, Denver, CO, 399-408.
7. Day-Lewis, F. D., Harris, J. M., and Gorelick, S. M., 2002, Time-Lapse inversion of crosswell radar data: Geophysics, vol. 67, 1740-1752.
8. Hausrath, E.M., Barrash, W., and Reboulet, E.C., 2002, Water sampling and analysis for the tracer/time-lapse radar imaging test at the Boise Hydrogeophysical Research Site: Center for Geophysical Investigation of the Shallow Subsurface Technical Report BSU CGISS 02-03, Boise State University, Boise, ID, 86 p.
9. Holliger, K., Musil, M., and Maurer, H. R., 2001, Ray-based amplitude tomography for crosshole georadar data: A numerical assessment: J. of Applied Geophysics, vol. 47, 285-298.
10. Hubbard, S.S., Peterson, J.E., Majer, E.L., Zawinslanski, P.T., Williams, K.H., Roberts, J., and Wobber, F., 1997, Estimation of permeable pathways and water content using tomographic radar data: Leading Edge, vol. 16, 1623-1628.
11. Lane, J. W. Jr., Haeni, F. P., and Day-Lewis, F.D., 1998, Use of time-lapse attenuation-difference tomography methods to monitor saline tracer transport in fractured crystalline bedrock: Proc., GPR '98, Seventh International Conf. on Ground Penetrating Radar: Lawrence, Kansas, USA, 533-538.
12. Lane, J. W. Jr., Day-Lewis, F.D., Harris, J. M., Haeni, F. P., and Goelick, S. M., 2000, Attenuation-difference radar tomography: Results of a multiple-plane experiment at the U. S. Geological Survey Fractured-Rock Research Site, Mirror Lake, New Hampshire: Proc., GPR 2000, Eighth International Conf. on Ground Penetrating Radar: Gold Coast, Australia, 666-675.
13. Liu, L., Lane, J. W., and Quan, Y., 1998, Radar attenuation tomography using the centroid frequency downshift method: J. of Applied Geophysics, vol. 40, 105-116.
14. Menke, W., 1989, Geophysical data analysis: discrete inverse theory. Academic Press, 289 p.
15. Peretti, W., Knoll, M. D., Clement, W. P., Barrash, W., and Pelton, J. R., 1999. GPR Imaging of complex fluvial stratigraphy at the Boise Hydrogeophysical Research Site: Proc., SAGEEP 1999 (Oakland, CA), EEGS, Denver, CO, 555-564.
16. Poeter, E. P. and McKenna, S. A., 1995, Reducing uncertainty associated with ground-water flow and transport predictions: Ground Water, vol. 33, 899-904.
17. Quan, Y. and Harris, J. M., 1997, Seismic attenuation tomography using the frequency shift method: Geophysics, vol. 62, 895-905.
18. Ramirez, A., Daily, W., Binley, A., LaBrecque, D., and Roelant, D., 1996, Detection of leaks in underground storage tanks using electrical resistivity tomography: J. Env. and Eng. Geophysics, vol. 1, no. 3, 189-203.
19. Reboulet, E.C., and Barrash, W., 1999, Identification of hydrostatigraphic facies in coarse, unconsolidated, braided-stream deposits at the Boise Hydrogeophysical Research Site (abs.): Geological Society America Annual Meeting, October 25-29, 1999, Denver, CO, Abs. with Prog., vol. 31., no. 7, p. A350.

20. Shapiro, A. M., Lane, J.R., Jr., and Olimpio, J.R., 1999, Borehole packers for in situ geophysical and microbial investigations in fractured rock: in Morganwalp, D.W., and Buxton, H.T., eds., U.S. Geological Survey Toxic Substances Hydrology Program--Proceedings of the Technical Meeting, Charleston, SC, March 8-12, 1999: U.S. Geological Survey-Water Resources Investigation Report 99-4018C, vol. 3, 841-845.
21. Slater, L.D., and Sandberg, S.K., 2000, Resistivity and induced polarization monitoring of salt transport under natural hydraulic gradients: Geophysics, vol. 65, 408-420.
22. Versteeg, R., Birken, R., Sandberg, S., and Slater, L., 2000, Controlled imaging of fluid flow and a saline tracer using time-lapse GPR and electrical resistivity tomography: Proc., SAGEEP 2000, (Arlington, VA), EEGS, Denver, CO, 283-292.
23. Zhou, B., and Fullager, F. K., 2001, Delineation of sulphide ore-zones by borehole radar tomography at Hellyer Mine, Australia: J. of Applied Geophysics, vol. 47, 261-269.
24. Zhou, C., Liu, L., and Lane, J.W., Jr., 2001, Nonlinear inversion of borehole-radar tomography data to reconstruct velocity and attenuation distribution in earth materials: J. of Applied Geophysics, vol. 47, 271-284.